

# Inverse Design of a Graphene-Based Quantum Transducer via Neuroevolution

Kevin Ryczko

*Department of Physics, University of Ottawa\* and  
Vector Institute for Artificial Intelligence, Toronto, Ontario, Canada*

Pierre Darancet<sup>†</sup>

*Center for Nanoscale Materials, Argonne National Laboratory, Lemont, IL 60439, United States and  
Northwestern Argonne Institute of Science and Engineering, Evanston, IL 60208, United States*

Isaac Tamblyn<sup>‡</sup>

*National Research Council of Canada  
Department of Physics, University of Ottawa\* and  
Vector Institute for Artificial Intelligence, Toronto, Ontario, Canada*

(Dated: March 10, 2022)

We introduce an inverse design framework based on artificial neural networks, genetic algorithms, and tight-binding calculations, capable to optimize the very large configuration space of nanoelectronic devices. Our non-linear optimization procedure operates on trial Hamiltonians through superoperators controlling growth policies of regions of distinct doping. We demonstrate that our algorithm optimizes the doping of graphene-based three-terminal devices for valleytronics applications, monotonously converging to synthesizable devices with high merit functions in a few thousand evaluations (out of  $\simeq 2^{3800}$  possible configurations). The best-performing device allowed for a terminal-specific separation of valley currents with  $\simeq 93\%$  valley purity. Importantly, the devices found through our non-linear optimization procedure have both higher merit function and higher robustness to defects than the ones obtained through geometry optimization.

## I. INTRODUCTION

Tailoring the properties of nanoelectronics devices leveraging quantum phenomena without classical analog is central to spintronics [1], valleytronics [2], quantum transduction, quantum sensing, and quantum computing [3–6]. The figure of merit of such nanoelectronics devices strongly depends on the details of the low-energy Hamiltonian and can be impacted by numerous energy scales. For example, in the case of graphene-based devices [7], valley-polarized currents can be manipulated spatially by tuning the edges of the devices, [8, 9], through strain-engineering, [10–20], defect-engineering, [21, 22], and by the combination of edge termination and doping. [8, 23–26]. While these studies predict high valley-filtering (e.g. with valley purity exceeding  $\sim 95\%$  [8]), actual, synthesizable, devices will display a superposition of these effects, resulting in a complex optimization process of these possibly-competing energy scales.

Such optimization is an inverse design problem, where one knows the desired output of the device, as defined by a simple merit function (e.g. valley or spin purity, current magnitude, etc.), but does not know the optimal way to modify the device under experimental and synthesizability constraints to obtain local or global extrema of these merit functions. Due to their large tunability and the number of atoms they contain (typically exceeding

$10^3$ ), the configuration space of nanoelectronic devices is extremely large and impossible to fully explore with high-throughput forward quantum transport solvers [27, 28]. In this context, the coming-of-age of artificial intelligence approaches capable of optimizing in large configuration space [29] offers significant opportunities. Local optimization techniques were used, for example, to design physically-unintuitive demultiplexer devices [30, 31] and chemical compounds [32].

Efficiently searching through large configuration spaces generally implies sampling a lower-dimensional space that maps to the original, higher dimensional, search space, possibly constructing this mapping with machine learning [33]. Another possibility is to use simple policies that yield complex outcomes, mimicking non-linear optimization processes observed in nature. In the work of Schelling [34], the complex dynamics of segregation was modeled by subtle changes in the underlying policies. This was also shown to be the case by Wolfram [35] on cellular automata. The use of a genetic algorithm (GA) to search through a large configuration space is common and has both advantages and disadvantages. GAs are gradient-free, are less likely to be trapped in local minima, and converge rapidly. On the contrary one must have a flexible ansatz (or set of genes) to fully describe the configuration space, gradients can not be used (if they are available), and it is difficult to include a feasibility of fabrication score in the objective function. This could result in finding optimal structures with a GA that could not be fabricated in the laboratory. This issue is eliminated for generative machine learning models where gradients are used to minimize an objective func-

---

\* kevin.ryczko@uottawa.ca

† pdarancet@anl.gov

‡ isaac.tamblyn@nrc.ca

tion. Machine learning models are flexible with respect to input and ability to learn complex mappings, but one must initially train the model and be confident in the model's ability to perform inference over a wide range of structures.

In this work, we demonstrate inverse design of nano-electronic devices using growth policies coupled to artificial neural networks (ANNs), GAs, and tight-binding calculations. Our framework is capable to navigate the very large configuration space through a non-linear optimization procedure that operates on trial Hamiltonians through a superoperator, effectively controlling growth policies of regions of distinct doping. We demonstrate optimization of the doping profile of graphene-based three-terminal devices for valleytronics applications, monotonously converging to synthesizable devices with high merit functions in a few thousand evaluations (out of  $\simeq 2^{3800}$  possible configurations). The predicted devices allow for terminal-specific separation of valley currents with a maximum of  $\simeq 93\%$  valley purity. Importantly, the devices found through our non-linear optimization procedure have both higher merit function and higher robustness to defects than the ones obtained through linear geometrical optimization [36].

In Section II, we detail our theoretical approach which includes the structure design, optimization procedure, and the methodology for calculating valley polarized currents. In Section III, we show that our optimization procedure produces structures that can separate valley polarized currents and analyze the GA optimization procedures.

## II. METHODS

Our general workflow is summarized in Fig.1, and consist of a structure generation scheme using an ANN, a (forward) quantum transport solver, and a GA.

Our framework operates on a fixed device structure, as represented by a graph Hamiltonian with a fixed adjacency matrix. Each vertex of the graph represents an orbital contributing to the low-energy Hamiltonian.

Each vertex has a corresponding on-site energy and a set of nearest neighbour couplings with sites defined in the adjacency matrix. The Hamiltonian of the system is

$$H = \sum_{\langle i,j \rangle} \tau_{ij} |i\rangle \langle j| + \sum_i U_i |i\rangle \langle i|, \quad (1)$$

where the first summation of Equation 1 describes the nearest neighbour interactions between orbitals  $i$  and  $j$ , and the second summation describes the on-site potential. The device is contacted to ballistic terminals with a predefined set of undoped lattice sites.

We focus on the case of three-terminal devices comprised of 3846 sites on a model of doped graphene, using

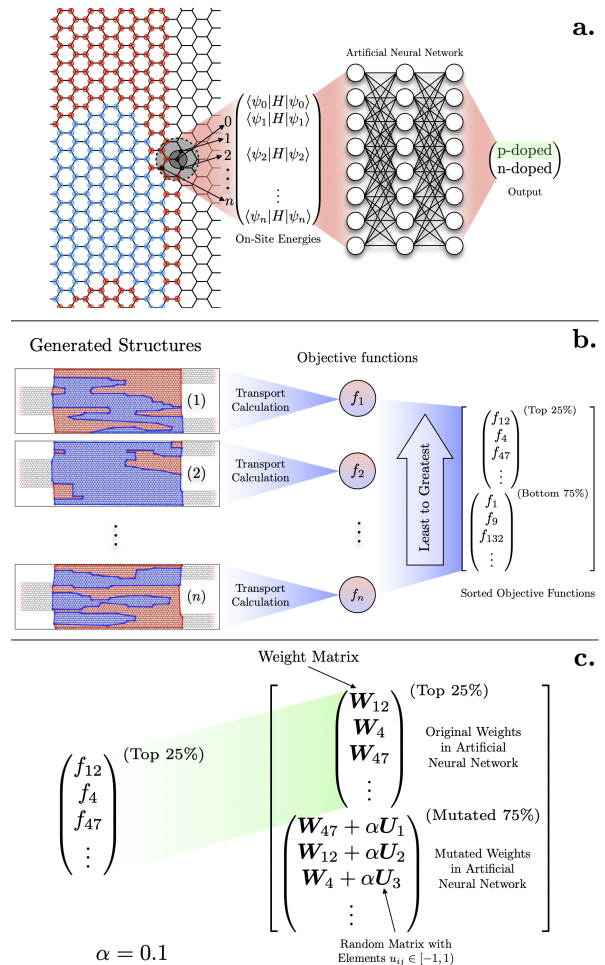


FIG. 1. Schematic description of optimization procedure. Starting from a trial Hamiltonian (consisting of either p- or n-doped regions on a fixed device lattice) (a), an artificial neural network policy is used to modify the on-site energy based on the on-site energies of its neighboring sites (nearest and next-nearest neighbors). The on-site energies for this set of lattice sites are concatenated into an input vector which is fed into an ANN policy that determines whether the selected lattice site will be p- or n-doped. The resulting merit function of each trial structure is then computed with a tight-binding transport solver [27] (b). The structures were taken from a random optimization procedure, with regions of n- and p-doping highlighted for clarification. The structures are then ranked based on their objective functions. The structures in the next generation are produced (c) using a genetic algorithm on the policies of the top 25% of the performers in the population of previous generations.

$\tau_{ij} = -2.7$  eV as done in [7], and

$$U_i = \begin{cases} U & \text{n-doped} \\ -U & \text{p-doped} \\ 0 & \text{terminal} \end{cases} \quad (2)$$

with  $U = 0.2$  eV, in alignment with past work [37].

The spatial extent of the p- and n-doped regions

on a given device is the result of an ANN policy that outputs the probability of given lattice sites to be p- or n-doped, as we now describe.

At the first iteration, we set all of the on-site energies to  $U_i = 0.5$  eV. For each lattice site  $i$ , the on-site energy along with the on-site energies of its nearest and next-nearest neighbors are concatenated into an input vector  $\mathbf{v}_{\text{input}}$ . This choice of input vector is motivated by the structure of the nearest-neighbor tight-binding Hamiltonian.

This choice of input vector is equivalent to using a graph convolution layer [38, 39] where the weight matrix is shared amongst all atoms. The input vector  $\mathbf{v}_{\text{input}}$  is then fed into the ANN policy where the output of the ANN is a number  $p \in [0, 1]$ . A random number  $u_p \in [0, 1]$  is then drawn such that if  $p < u_p$  the site is p-doped, and n-doped otherwise. This ANN policy can also be thought of as a superoperator that operates on a constant tight-binding Hamiltonian yielding a Hamiltonian with a set of desired optimized properties. At each iteration, the weights of the ANN policy are updated using a GA in conjunction with the ANN [40, 41].

To avoid producing structures where the doping changes over a short length scale, we apply Gaussian blurring as well as binary erosion and dilation on binary images of the lattice (1(0) represented p(n)-doping).

The initialization stage of the optimization process consists of  $N = 160$  devices, each corresponding to a distinct ANN policy.

Given these  $N$  Hamiltonians, we calculate the valley-polarized currents using the Kwant Python package [27], through the following equation:

$$I_{K/K'} = \frac{e}{\pi h} \int_{-\infty}^{\infty} d\epsilon G_{K/K'} [f(\epsilon; \mu_L) - f(\epsilon; \mu_R)] \quad (3)$$

where  $G_{K/K'}$  is the valley-dependent conductance,  $f(E; \mu_{L/R})$  is the Fermi-Dirac function for the left ( $L$ ) and right ( $R$ ) leads,  $e$  is the electron charge, and  $h$  is Planck's constant. To calculate the valley-polarized conductance we use the Landauer-Büttiker formula

$$G_{K/K'} = \frac{2e^2}{h} \sum_{n_{\text{modes}, K/K'}} T_n, \quad T_n = \sum_{m_{\text{modes}}} |t_{nm}|^2 \quad (4)$$

where the sum over  $n_{\text{modes}, K/K'}$  are for incoming modes with momenta associated with valley  $K$  or  $K'$ , and the sum over  $m_{\text{modes}}$  are for all out going modes in the lead where we want to measure the current. Travelling modes (either  $K$  or  $K'$ ) are identified by considering their velocity and momentum, following [8]. The transmission probabilities  $T_n$  are computed after the determination of the scattering matrix. In addition, we use a bias of 0.5 eV and a grid spacing of 1 meV to evaluate the integral in Eq. 3 throughout all of our calculations.

We consider three-terminal devices with a non-valley-polarized current incoming from lead 0 (the “left” of the device in Fig. 1 b). At the opposite side of the device,

two leads 1 and 2 at identical chemical potentials collect the valley-dependent current injected from lead 0.

Before defining the objective function, we first define the purity of  $K'$  current in lead 1 to be  $P_{K',1} = I_{K',1}/(I_{K,1} + I_{K',1})$  and the purity of  $K$  current in lead 2 to be  $P_{K,2} = I_{K,2}/(I_{K,2} + I_{K',2})$ . We then define the normalized total current  $I_{\text{total}} = (I_{K',1} + I_{K,2})/I_P$  where  $I_P = 0.3 e/\pi h$  is the total current of the pristine graphene lattice. We search for structures that maximize the multivariate objective function:

$$F(I_{K,1}, I_{K',1}, I_{K,2}, I_{K',2}) = P_{K',1}^2 + P_{K,2}^2 + I_{\text{total}}^2 \quad (5)$$

We compute Eq. 5 for each of the  $N$  devices. Only the ANN policies associated with the top 25% devices are kept to populate the next generation, through random mutation of the weights of the ANN policy yielding a new device. We do not consider crossover mutations in our study.

The weights of the newly generated ANN policy are

$$\begin{pmatrix} w_1 \\ w_2 \\ \vdots \\ w_M \end{pmatrix}_{\text{new}} = \begin{pmatrix} w_1 \\ w_2 \\ \vdots \\ w_M \end{pmatrix}_{\text{old}} + \alpha \begin{pmatrix} u_1 \\ u_2 \\ \vdots \\ u_M \end{pmatrix} \quad (6)$$

where  $\alpha = 0.1$  is a small parameter (similar to a learning rate),  $u_i \in [-1, 1]$  is a random number, and  $M$  is the total number of weights. In our case we used ANNs with 2 hidden layers each with 128 neurons. The logistic activation function was used throughout the ANN. During the optimization process we ran calculations for 160 devices in parallel and performed 64 generations. The calculations performed for each generation took  $\simeq 45$  minutes on single node with 40 CPUs.

### III. RESULTS

The results of the optimization procedure are shown in Figure 2. We show the average and maximum optimization function, valley current purity, and associated valley currents for the best performing devices of each independent seed as a function of generation following Section II. We also show the associated standard deviation over the  $N = 64$  independent calculations. Both the averages of the objective function and purity of the valley currents converge monotonously across 64 generations. The optimization process produces structures with average (maximum) purity of both  $K$  and  $K'$  valley currents are  $\sim 87\%$  ( $\sim 93\%$ ). This result is comparable to Rycerz *et al.* [8] where they achieved  $\sim 95\%$  purity with an idealized valley filtering device.

The average purity of  $K$  valley current at generation 0, based on the random initialization is higher ( $> 80\%$ ) than the average purity of  $K'$  valley current for the best performing devices. In the remainder of the optimization process, the algorithm is capable to maintain the  $K$  valley current purity steady while increasing the value of the  $K'$

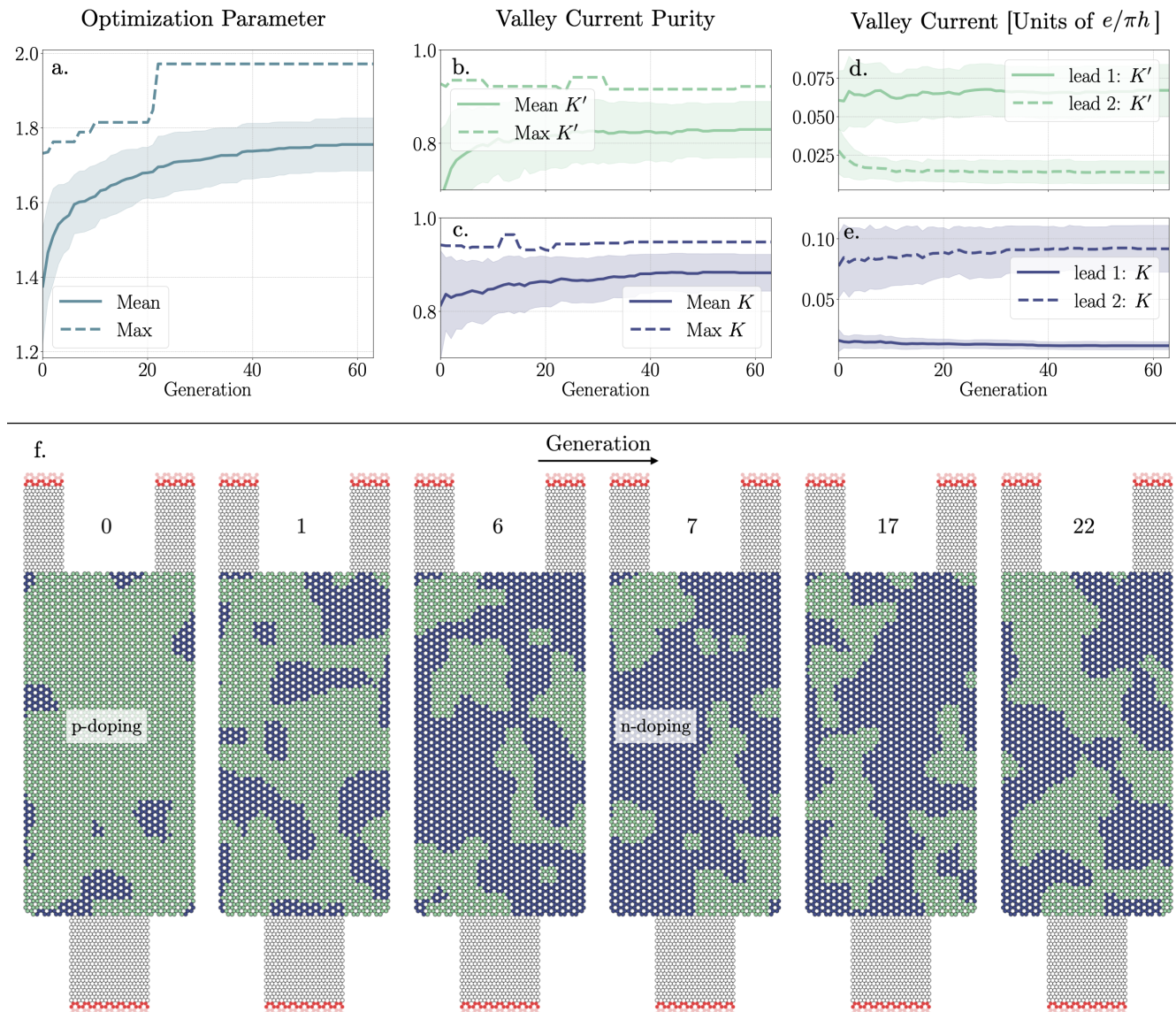


FIG. 2. Optimization function (a), valley current purity (b-c), and valley currents (d-g) recorded during the optimization processes using the artificial neural network policy. For each independent optimization, the devices with the maximum objective functions are recorded. The solid lines show the average values of these devices and the lighter regions show the standard deviations. In f. we show the evolution of best performing structures for one seed.

valley current purity, which started at an average value of  $\sim 70\%$  purity.

In addition to the convergence of the average currents, average measures of purity, and the average of the objective functions we also find that the standard deviation of the optimizations decreases as a function of generation. This indicates that the population is converging to a similar local maxima.

In Figure 2 f, we also show the evolution of the best-performing structures for a single seed.

To further understand the devices resulting from the optimization procedures, we investigate the doping profiles and their effects on valley currents. In particular, we perform similar optimizations as discussed in Section

II but only allow for either p- or n-doping, rather than both. In Figure 3 b-c we plot the likelihood that a given site would have p- or n-doping when the valley currents are optimized. The likelihood comes from averaging over the final structures from the 64 optimizations with different seeds. We see the algorithm prefers uniform doping directly in contact with the leads, with the p(n)-doping acting as a waveguide for the  $K'(K)$  valley current towards lead 1 (2). Each choice of doping guides one of the valley currents and has little effect on the other valley current. In the case of p(n)-doping, the  $K(K')$  valley current had a valley current purity of  $\simeq 57\%$ . In addition to these experiments, we also performed calculations to optimize either  $K$  or  $K'$

purity, allowing for both p- and n-doping, and following the same protocol as described in Section II. We found that we could reach 96% purity for  $K'$  and 97% purity for  $K$ , which is on-par with the valley purity reported previously [8].

In contrast with this doping-induced behavior for single valley polarization, devices optimized using Eq. 5 shows mixed doping in front of lead 0, and weak long-range order, as shown in Fig 3. To quantify to length scale of the ordering of the devices found by optimizing Equation 5, we calculated pair correlation functions (PCFs)  $g(r)$  where the atom types are labelled by their respective doping. The PCFs were also normalized by the Carbon-Carbon PCF. If  $g(r)/g_{CC}(r) \approx 1$ , then we expect to see uniform doping across the crystal. If  $g(r)/g_{CC} \approx 0$ , then we expect to see non-uniform doping across the crystal. For  $g_{pp}(r)/g_{CC}(r)$  and  $g_{nn}(r)/g_{CC}(r)$ , we find that the values decrease from 1 as  $r$  increases. Therefore if we have a site that is p(n)-doped, we expect adjacent sites to be p(n)-doped for up to 10 Å with high probability. Beyond 10 Å, there is a  $\sim 50\%$  chance to see a p(n)-doped site given p(n)-doped site is selected, indicating seemingly random arrangement.

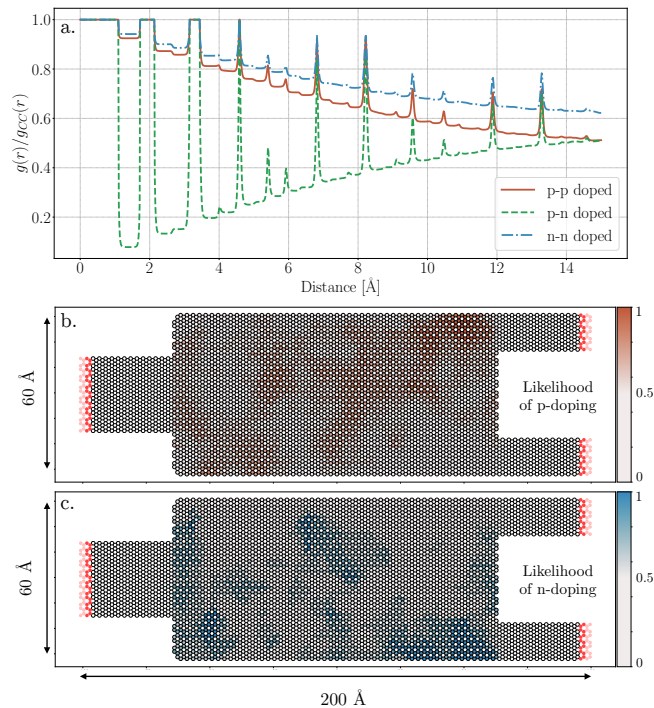


FIG. 3. Pair correlation functions (PCFs -  $g(r)$ ) divided by the PCF of graphene ( $g_{CC}(r)$ ) where p- and n-doping are considered to be different atoms (a). Likelihood of finding a given lattice site with p-doping (b) and likelihood of finding a given lattice site with n-doping (c) for the optimizations where sites were either p(n)-doped or undoped.

We note that this characteristic 10 Å length exceeds the information from neighbors and next-nearest neighbors

given to the superoperator, and are a result of the ANN encoding and the growth policy; the local environment encoded in the input vectors overlap allowing information to be propagated. The same effect can be seen when machine learning potential energy surfaces using fingerprint functions to describe atomic environments [42, 43]. These fingerprint functions have a cut-off radius that may be smaller than a certain interaction distance (i.e. vdW interactions), but because of the overlap of the fingerprints, they still can describe interactions that exceed the cut-off radius.

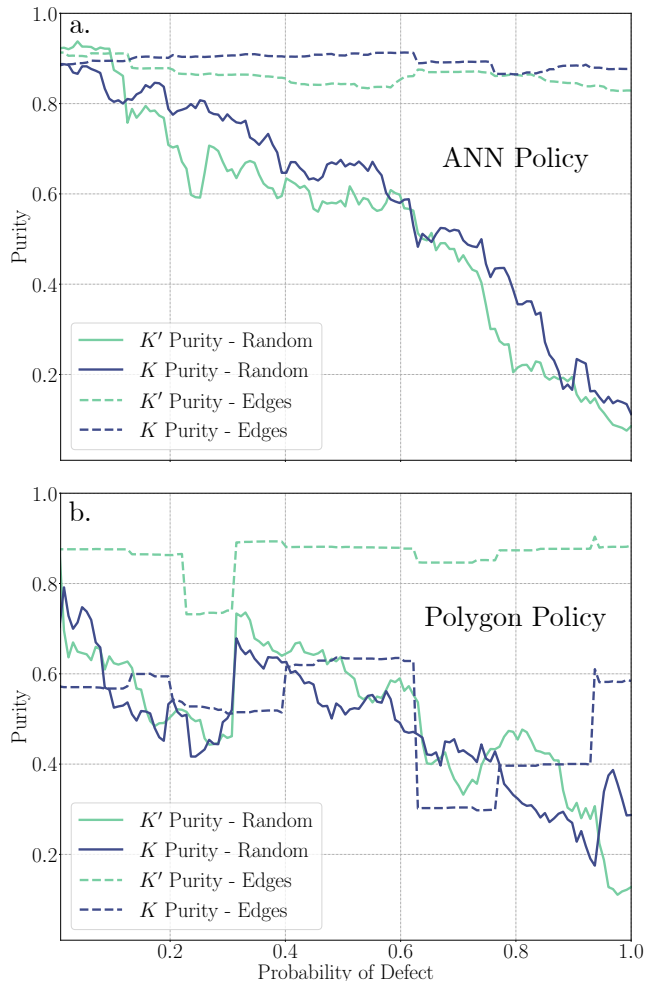


FIG. 4. Purity of the most optimal device as a function of the probability that a lattice site will have a defect (flipped doping). Solid curves are for randomly selected sites and dashed curves are for sites separating p-doped regions from n-doped regions (edge sites). The top plot is for the ANN policy (a), and the bottom plot is for the polygon policy (b). See Section II for more information on the ANN policy and the supplemental information [36] for more information on the Polygon policy.

Lastly, we investigate the sensitivity of the generated structure that had the maximum objective function. To do so, we consider two protocols. In the first proto-

col that we refer to as the ‘random’ protocol, we scan through every lattice site and flip the doping (p- to n-doping or vice versa) of the site if  $u < p$  where  $u$  is a randomly generated number  $u \in [0, 1)$  and  $p$  is the probability that the doping will be flipped. In the second protocol, we only consider flipping the doping of lattice sites that separate p-doped regions from n-doped regions. We refer to these lattice sites as ‘edges’ and refer to this protocol as the ‘edge’ protocol.

In Figure 4, we show the purity of the valley currents as a function of the probability  $p$  for the ANN policy outlined in Section II as well as our polygon policy outlined in the supplemental information [36]. For the ANN policy with the random protocol, we find that the purity of both  $K$  and  $K'$  valley currents decrease linearly (with noise) as a function of the probability  $p$ . This is in agreement with [8], where random vacancies were introduced in the lattice. For the ANN policy with the edge protocol, we find that the purity remains almost constant, with a slight decay as the probability  $p$  increases. This indicates that the proposed structure is robust to changes around the edges of p- or n-doped regions.

In contrast, for the polygon policy with the random protocol we find a decrease of the purity of valley currents as a function of the probability  $p$ , but with large steps at certain values of  $p$ . These large jumps in purity are also observed for the polygon policy with the edge protocol. These large and random jumps in the purity indicate the sensitivity of this protocol. Electron waves can be focused and split, similar to light waves, depending on the shape of the doped regions [23, 25]. When one changes the curvature of a lens slightly, the behavior of light can be drastically different. A similar process is occurring here with the electron waves.

#### IV. CONCLUSION

In conclusion, we describe a technique that uses genetic algorithms and artificial neural network policies to optimize the purity of valley currents in graphene nanodevices with pn-doping. This optimization strategy operates on a tight-binding Hamiltonian and yields a new,

optimized Hamiltonian for our objective function. This technique allows for rapid convergence of the optimization parameter studied, and yields similar solutions from independent calculations with different seeds. After averaging over an ensemble of optimization procedures we have found that p(n)-doping acts as a waveguide for  $K'(K)$  valley current, allowing one to physically separate valley currents in graphene nanoribbons. After averaging over the ensemble of optimization procedures with both p- and n-doping, we found that the maximum purity of the valley currents were  $\simeq 93\%$ . When averaging over the ensemble of optimization procedures with only p(n)-doping, we found that the purity of  $K'(K)$  valley remains at  $\simeq 93\%$ . This shows that p(n)-doping acts as a guide to  $K'(K)$  valley current. We also achieve a valley purity of 96% for  $K'$  and 97% for  $K$  current when only optimizing one valley. Additionally, we found that the artificial neural network policy can produce structures with long-range order despite only having local information. We also performed sensitivity analysis which showed that the proposed optimal structure of the artificial neural network policy is robust to edge defects. Such a device could be used to convert a quantum state to a digital signal.

#### V. ACKNOWLEDGMENTS

KR and IT acknowledge funding from the Natural Sciences and Engineering Research Council of Canada. Work at the National Research Council was carried out under the auspices of the AI4Design Program. KR and IT acknowledge Compute Canada for computational resources. This material is based upon work supported by Laboratory Directed Research and Development (LDRD) funding from Argonne National Laboratory, provided by the Director, Office of Science, of the U.S. Department of Energy under Contract No. DE-AC02-06CH11357. Use of the Center for Nanoscale Materials, an Office of Science user facility, was supported by the U.S. Department of Energy, Office of Science, Office of Basic Energy Sciences, under Contract No. DE-AC02-06CH11357.

- 
- [1] S. Bader and S. Parkin, *Annu. Rev. Condens. Matter Phys.* **1**, 71 (2010).
  - [2] J. R. Schaibley, H. Yu, G. Clark, P. Rivera, J. S. Ross, K. L. Seyler, W. Yao, and X. Xu, *Nature Reviews Materials* **1**, 16055 (2016).
  - [3] K. F. Mak, K. He, J. Shan, and T. F. Heinz, *Nature Nanotechnology* **7**, 494 (2012).
  - [4] H. Zeng, J. Dai, W. Yao, D. Xiao, and X. Cui, *Nature Nanotechnology* **7**, 490 (2012).
  - [5] T. Cao, G. Wang, W. Han, H. Ye, C. Zhu, J. Shi, Q. Niu, P. Tan, E. Wang, B. Liu, and J. Feng, *Nature Communications* **3**, 887 (2012).
  - [6] K. F. Mak, K. L. McGill, J. Park, and P. L. McEuen, *Science* **344**, 1489 (2014).
  - [7] A. H. Castro Neto, F. Guinea, N. M. R. Peres, K. S. Novoselov, and A. K. Geim, *Reviews of Modern Physics* **81**, 109 (2009).
  - [8] A. Rycerz, J. Tworzydło, and C. W. J. Beenakker, *Nature Physics* **3**, 172 (2007).
  - [9] D. Xiao, W. Yao, and Q. Niu, *Physical Review Letters* **99**, 236809 (2007).
  - [10] N. Levy, S. Burke, K. Meaker, M. Panlasigui, A. Zettl, F. Guinea, A. C. Neto, and M. Crommie, *Science* **329**, 544 (2010).

- [11] F. Guinea, B. Horovitz, and P. Le Doussal, *Physical Review B* **77**, 205421 (2008).
- [12] M. Settnes, S. R. Power, and A.-P. Jauho, *Physical Review B* **93**, 035456 (2016).
- [13] M. Settnes, S. R. Power, M. Brandbyge, and A.-P. Jauho, *Physical review letters* **117**, 276801 (2016).
- [14] D. Zhai and N. Sandler, *Physical Review B* **98**, 165437 (2018).
- [15] T. Stegmann and N. Szpak, *New Journal of Physics* **18**, 053016 (2016).
- [16] Y. Wu, D. Zhai, C. Pan, B. Cheng, T. Taniguchi, K. Watanabe, N. Sandler, and M. Bockrath, *Nano letters* **18**, 64 (2017).
- [17] E. Andrade, R. Carrillo-Bastos, and G. G. Naumis, *Physical Review B* **99**, 035411 (2019).
- [18] Y. Hatsugai, *JPSJ News and Comments* **16**, 13 (2019).
- [19] A. McRae, G. Wei, and A. Champagne, *Physical Review Applied* **11**, 054019 (2019).
- [20] T. Fujita, M. Jalil, and S. Tan, *Applied Physics Letters* **97**, 043508 (2010).
- [21] D. Gunlycke and C. T. White, *Physical Review Letters* **106**, 136806 (2011).
- [22] J.-H. Chen, G. Autès, N. Alem, F. Gargiulo, A. Gautam, M. Linck, C. Kisielowski, O. Yazyev, S. Louie, and A. Zettl, *Physical Review B* **89**, 121407 (2014).
- [23] V. V. Cheianov, V. Falko, and B. L. Altshuler, *Science* **315**, 1252 (2007).
- [24] C. Park, *Physical Review Applied* **11**, 044033 (2019).
- [25] J. Garcia-Pomar, A. Cortijo, and M. Nieto-Vesperinas, *Physical review letters* **100**, 236801 (2008).
- [26] T. Aktor, J. H. Garcia, S. Roche, A.-P. Jauho, and S. R. Power, *arXiv preprint arXiv:1910.00489* (2019).
- [27] C. W. Groth, M. Wimmer, A. R. Akhmerov, and X. Waintal, *New Journal of Physics* **16**, 63065 (2014).
- [28] S. Steiger, M. Povolotskyi, H.-H. Park, T. Kubis, and G. Klimeck, *IEEE Transactions on Nanotechnology* **10**, 1464 (2011).
- [29] D. Silver, J. Schrittwieser, K. Simonyan, I. Antonoglou, A. Huang, A. Guez, T. Hubert, L. Baker, M. Lai, A. Bolton, *et al.*, *Nature* **550**, 354 (2017).
- [30] A. Y. Piggott, J. Lu, K. G. Lagoudakis, J. Petykiewicz, T. M. Babinec, and J. Vučković, *Nature Photonics* **9**, 374 (2015).
- [31] L. Su, A. Y. Piggott, N. V. Sapra, J. Petykiewicz, and J. Vukovi, *ACS Photonics* **5**, 301 (2018), <https://doi.org/10.1021/acsp Photonics.7b00987>.
- [32] R. Leardi, *Journal of Chemometrics: A Journal of the Chemometrics Society* **15**, 559 (2001).
- [33] D. Melati, Y. Grinberg, M. K. Dezfouli, S. Janz, P. Cheben, J. H. Schmid, A. Sánchez-Postigo, and D.-X. Xu, *Nature communications* **10**, 1 (2019).
- [34] T. C. Schelling, *The Journal of Mathematical Sociology* **1**, 143 (1971).
- [35] S. Wolfram, *Reviews of Modern Physics* **55**, 601 (1983).
- [36] *Supplemental Information* (2020).
- [37] K. Wakabayashi and T. Aoki, *International journal of modern physics B* **16**, 4897 (2002).
- [38] D. K. Duvenaud, D. Maclaurin, J. Iparraguirre, R. Bombarell, T. Hirzel, A. Aspuru-Guzik, and R. P. Adams, in *Advances in Neural Information Processing Systems 28*, edited by C. Cortes, N. D. Lawrence, D. D. Lee, M. Sugiyama, and R. Garnett (Curran Associates, Inc., 2015) pp. 2224–2232.
- [39] T. N. Kipf and M. Welling, *arXiv preprint arXiv:1609.02907* (2016).
- [40] C. Beeler, U. Yahorau, R. Coles, K. Mills, S. Whitelam, and I. Tamblyn, *arXiv preprint arXiv:1903.08543* (2019).
- [41] F. P. Such, V. Madhavan, E. Conti, J. Lehman, K. O. Stanley, and J. Clune, *arXiv preprint arXiv:1712.06567* (2017).
- [42] J. Behler and M. Parrinello, *Physical review letters* **98**, 146401 (2007).
- [43] K. T. Schütt, H. E. Sauceda, P.-J. Kindermans, A. Tkatchenko, and K.-R. Müller, *The Journal of Chemical Physics* **148**, 241722 (2018).